Polish Journal of Medical Physics and Engineering
The Journal of Polish Society of Medical Physics
ISSN 1898-0309, doi: 10.2478/pjmpe-2025-0039

December 2025
Vol 31, Issue 4

Technical Note

Tailored software for post-radiotherapy lung radiomics analysis

Marek Fechner[1,CDF*], Marek Konkol[2,3,ABEF], Marcin Wiktorowski[1,BCDF], Piotr Miklosik[1,EF], Paweł Śniatała[1,ACEF]

[1]*Faculty of Computing and Telecommunications, Poznan University of Technology, Poznan, Poland*
[2]*Department of Electroradiology, Poznań University of Medical Sciences, Poznan, Poland*
[3]*Radiation Oncology Department IV, Greater Poland Cancer Centre, Poznan, Poland*
**Corresponding author: Marek Fechner; marek.fechner@put.poznan.pl*

(received 25 October 2025; revised 24 November 2025; accepted 30 November 2025)

Abstract

Introduction: Radiotherapy is a crucial method of treating lung cancer. However, potential toxicity such as radiation-induced lung injury (RILI) must be considered. In order to quantitatively describe different forms of RILI, a next generation of a previously discussed system has been developed to analyse the subsequent series of CT scans performed by patients during radiation therapy and post-RT follow-up.

Materials and methods: A 3D CT scan registration module has been developed as part of the system. The analysis management module has been expanded compared to previous versions of the system. The environment has been prepared and the system has been deployed. In order to determine the effectiveness of the system, 1598 analyses, based on automated image pre-processing (registration and segmentation) and first-order delta-radiomics features, have been performed on a data set from 50 Patients.

Results: The efficiency of the execution of the analysis was evaluated in terms of time, including a breakdown into individual stages of the pipeline. The results of the analyses were visualised and exported to a CSV file, then evaluated from a clinical perspective.

Conclusions: The system allows, thanks to the use of a 3D registration algorithm, to analyse changes more accurately than before, and thanks to the use of a more flexible architecture, to introduce subsequent registration and calculation algorithms more easily. The current main research and development areas of the system include the extension of the analytical capabilities of the system in the field of radiomics and the expansion of the number of image analysis algorithms used within the system.

Keywords: lung cancer, CT images analysis, pulmonary fibrosis, radiotherapy, 3D image registration, radiation-induced lung injury, first-order features radiomics

1. Introduction

Cancer is becoming more and more common throughout the world, for many reasons, including ageing of the population and population growth[1]. In particular, lung cancer is indicated as the second most frequently diagnosed malignancy after skin cancer, the most common cause of cancer-related deaths in men and the second most common cause of cancer-related deaths within women, according to 2017 data[2,3].

Approximately 50% of patients diagnosed with lung tumours undergo radiation therapy at some stage of treatment[4]. Modern radiotherapy uses highly precise conformal dose delivery methods such as SBRT (Stereotactic Body Radiotherapy), IMRT (intensity modulated radiation therapy), or VMAT (Volume arc technique)[5]. However, regardless of the form of radiation delivery used, potential toxicity must be taken into account. The common term Radiation-induced lung injury (RILI) includes the early inflammatory response of lung tissue known as radiation-induced pneumonitis (RIP) which occurs within the first six months after the radiotherapy, and the radiation-induced lung fibrosis (RILF) – a late chronic complication that can lead to dyspnea and decreased respiratory function[6-9]. The literature provides a wide range of 5% to 58% of the occurrence of RIP in patients undergoing chest radiotherapy[10]. RILF is less frequently reported, with a 30% incidence for the IMRT method[11]. RILI can be asymptomatic and life-threatening[9]. Presentation of RIP can vary from subclinical radiographic findings, mild symptoms (general fatigue, dry, non-productive cough) to a life-threatening disease that requires hospitalisation (respiratory failure). Extensive RILF

Authors' contribution: A – Research concept and design, B – Collection and/or assembly of data, C – Data analysis and interpretation, D – Writing the article, E – Critical revision of the article, F – Final approval of the article.

can present as progressive dyspnea, developing pulmonary hypertension and cor pulmonale[12].

Therefore, further research is still needed to understand this toxicity. An approach, known as radiomics, is to extract quantitative features or texture – the so-called radiomic features – from medical images, to decode tissue pathology or predict the outcome[13].

There is a wide range of post-RT image findings. During the early phase there are mainly ground-glass and reticular opacities progressing to airspace mass-like and scar-like consolidation and traction bronchiectasis[14]. Late fibrosis radiologically presents as sharply defined consolidation or linear scarring with volume loss and architectural distortion[15].

There are different clinical scales to assess RILI. The most used are CTCAE v5.0 (Common Terminology Criteria for Adverse Events, version 5.0), LENT-SOMA (Late Effects in Normal Tissue-Subjective Objective Management Analysis), RTOG (Radiation Therapy Oncology Group) and SWOG (Southwest Oncology Group).

However, the unclear and subjective nature of the scales hinders the comparison of research results, especially in subclinical patients. Hence, there is a need to establish quantitative methods of the assessment. The change in lung tissue density expressed in Hounsfield units (HU) derived from CT scans can be a numeric surrogate of the radiologist's eye, as it appears to fit the most implemented NTCP models of lung radiation[16]. Furthermore, some authors showed a dose-response relation and evolution over time that confirm the first-order radiomic approach[17-22].

Therefore, our objective was to develop a delta radiomic tool to determine the relationship between the dose administered and the incidence of RILI in patients with lung cancer. For this purpose, a system was developed to compare CT scans at different time points to observe changes in lung tissue density based on differences in Hounsfield unit values[23]. The results obtained were then clinically analysed and a dose-effect relationship was demonstrated using a sigmoidal model. It was also confirmed that the evolution of changes in time corresponds to a typical clinical presentation of radiation-induced toxicity[24].

The purpose of this document is to present the current state of the system and the changes introduced, in particular regarding the modification of the registration algorithm, the preparation of the system for other registration algorithms, and the introduction of a pipeline for the mechanics of CT scan analysis.

The document has the following structure. First, similar works are briefly described. Next, the general current architecture of the system is characterised. Then, the current analysis pipeline, results visualisation and analysis efficiency is discussed. The last part concludes the document.

2. Similar works

To the best of the authors' knowledge, it may be difficult to find many works with the same subject matter as the one presented in this article. However, a number of works can be identified with similar topics, i.e., those concerning automatic analysis of CT scans using radiomic features in the field of pulmonary oncology. Some of these studies consider the issue of pulmonary nodule detection or classification. For example[25], discusses the development of a model to distinguish between lung adenocarcinoma (ADC) and squamous cell carcinoma (SCC) based on CT scan analysis. Similar issues concerning the automation of distinguishing between ADC and SCC are discussed in[26], with the additional assumption of solid elements > 8 mm. Three approaches are compared: an approach based on radiomic features, an approach based on radiological features, and a combined approach. In the study[27] the effectiveness of localization of lung nodules is compared, using an automatic model based on convolutional networks (CNN) and an indication of an expert group. In the study[28], the authors classified solitary pulmonary nodules, between malignant and benign, according to radiomic features.

The literature also includes a number of works on the use of CT scan analysis in the context of the adopted therapy model. For example, for SBRT, studies can be found on developing predictions of potential therapy effectiveness and the possibility of disease recurrence based on clinical data and radiomic analysis of CT scans[29,30]. In this context, for neoadjuvant chemoimmunotherapy, for example, works on the prediction of the body response to applied treatment can be found[31,32]. In the field of surgical treatment, for example, a paper on determining the usefulness of a radiomic system can be indicated in the context of evaluating the preoperative tumour aggressiveness index in stage I lung adenocarcinoma (ADC) with a diameter of <= 2 cm [33] and a paper on predicting the risk of postoperative brain metastases for non-small cell lung cancer (NSCLC) based on radiographic characteristics[34].

3. High-level view of the system architecture

3.1. Architecture overview

Designing the architecture of systems containing more complex algorithmic mechanisms may involve additional challenges. For the part of the system responsible for interaction with the User, all classic system requirements are still important, such as: UX/UI, testability, security, performance, availability, or fault tolerance, while in the algorithmic part of the system additional factors such as accuracy, flexibility in the selection of the algorithm, quality of data and the resulting solution, concurrency, or the ability to easily carry out subsequent iterations of experiments might be also important. For this reason, a solution that can positively influence the quality of architecture may be to separate the part of the system responsible for algorithms from the part responsible for interactions with the user, while maintaining the possibility of communication between them[35].

This path was adopted as part of the development of the system, in the **Figure 1**: Lungs Radiomics Project – context diagram a high-level view of the system architecture can be found. There are two main subsystems within the system:

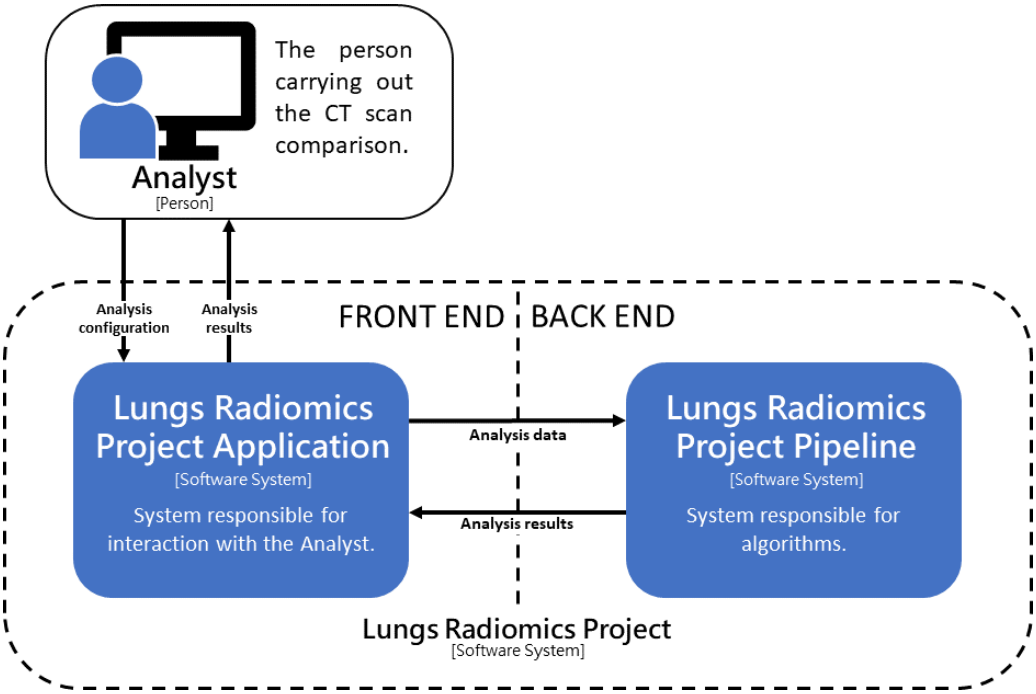

Figure 1. Lungs Radiomics Project – context diagram.

- Lungs Radiomics Project Application – a subsystem responsible for enabling the user to configure input data of analyses and review their results,
- Lungs Radiomics Project Pipeline – a subsystem responsible for conducting analyses and transferring the obtained results back so that they become available to the user in a friendly form.

Within the meaning of the C4 model[36], the following containers can be indicated as part of the Lungs Radiomics Project Application subsystem (**Figure 2**: Lungs Radiomics Project Application – container diagram). As can be seen, the Lungs Radiomics Project Application consists of two containers, a database used to store analysis configuration data, and a web application through which the user can interact with the system.

The Lungs Radiomics Project Pipeline subsystem in an analogous diagram is presented in **Figure 3**: Lungs Radiomics Project Pipeline – container diagram. It can be seen that for pipeline orchestration, Dagster[37] was used, supported by the MariaDB[38] database.

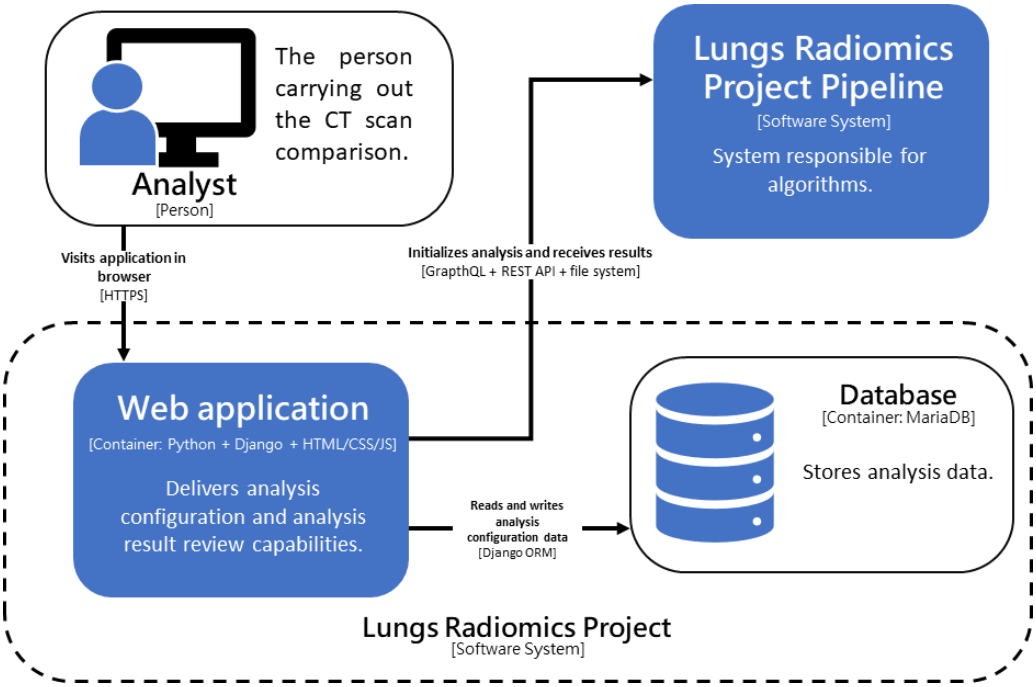

Figure 2. Lungs Radiomics Project Application – container diagram.

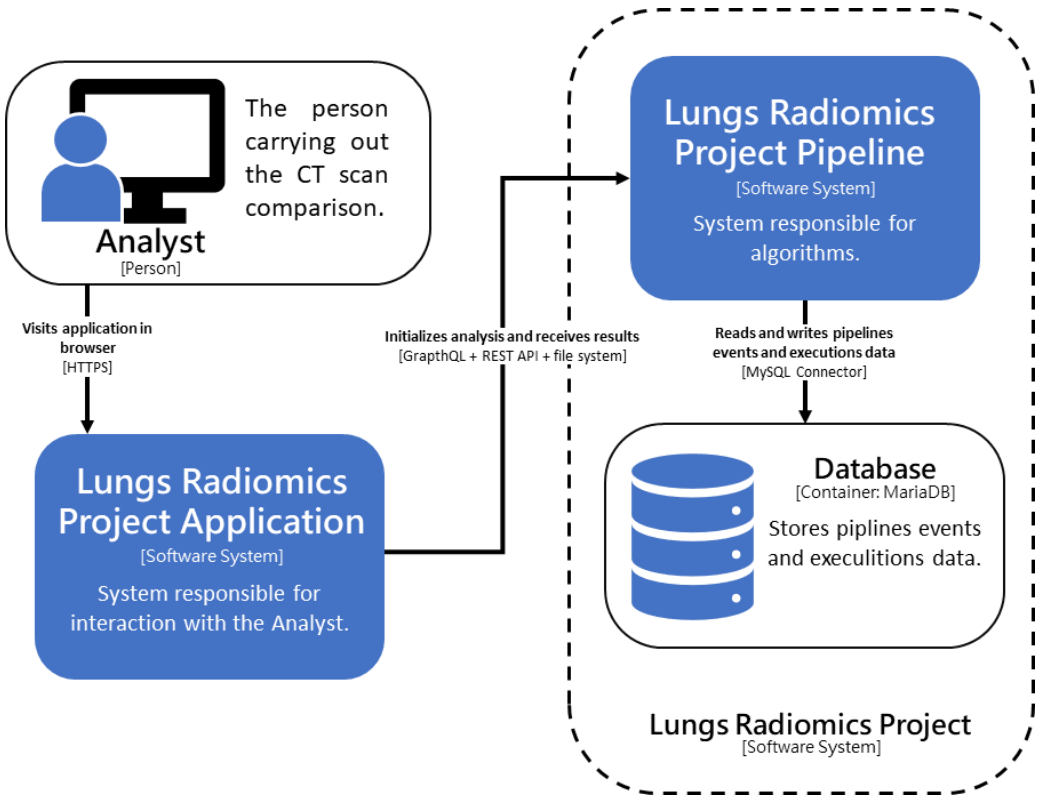

Figure 3. Lungs Radiomics Project Pipeline – container diagram.

3.2. Technology stack

The entire analysis pipeline was implemented in Python[39] due to its wide applicability in scientific fields and therefore a particularly important feature from the perspective of the present study: a wide range of tools to process medical images.

The SimpleITK[40] library was used as the primary image processing tool. It is an image analysis toolkit with a large number of components that support general filtering operations, image segmentation, and registration. It supports processing of multidimensional spatio-temporal images: 2D, 3D, and 4D in many formats, ranging from first class standards in medical applications such as Digital Imaging and Communications in Medicine (DICOM), Neuroimaging Informatics Technology Initiative (NIfTI) to common image storage formats (JPG, PNG, TIFF). SimpleITK itself is written in C++ for high efficiency, but it is also packaged in many popular languages such as Python, Java, or C#. A key feature of SimpleITK is that unlike standard image processing libraries, it operates in physical space, i.e. an image is defined as a set of points on a grid corresponding to some region in physical space. This differs significantly from many other image analysis libraries that represent an image as a plain pixel/voxel array, which implies no concept of representation of the image in physical space and thus assumes isotropic pixel spacing.

A critical aspect of 3D image processing is the ability to efficiently process large volumes of data. Therefore, Dagster was chosen as the tool for orchestrating data processing pipelines. Dagster is a powerful data orchestration tool that provides a comprehensive set of features for building and managing complex data processing pipelines, including parallel job execution, defining pipelines as directed acyclic graphs (DAGs), job monitoring, various deployment scenarios, configuration options, job queuing, and failed job rescheduling. Dagster uses DAGs, which are a directed acyclic graph of tasks that describe the steps of a pipeline. The graph specifies the dependencies between pipeline steps, ensuring that the pipeline executes tasks in parallel in the correct order. Dagster automatically distributes the work across multiple cores, machines, or clusters, allowing efficient processing of large volumes of data. This feature helps to significantly reduce the processing time.

4. Analysis pipeline steps

The main stages of the analysis are presented in **Figure 4**: Analysis – main flow diagram. In particular, the following stages can be distinguished as follows:

- providing input data and analysis parameters configuration,
- application pre-registration and registration algorithms for the given pair of scans,
- extraction of desired regions based on segmented lungs, radiation doses, and optionally selected contours,
- performing calculations and exporting analysis results,
- displaying analysis results for further review.

These steps will be described in the following sections.

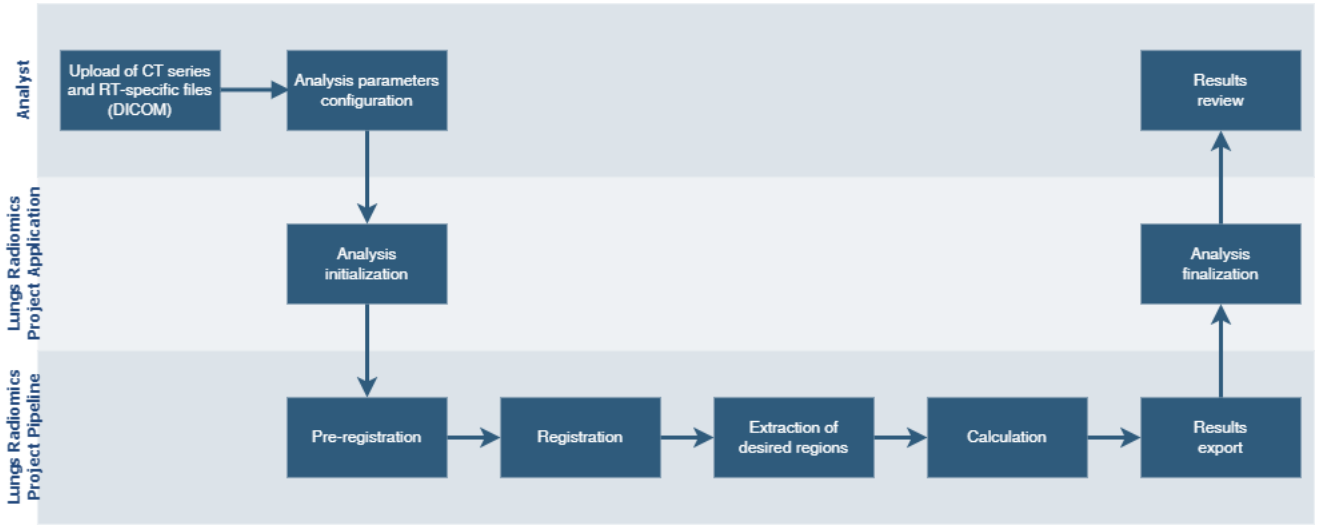

Figure 4. Analysis – main flow diagram

4.1. Input data and analysis parameters configuration

The first stage of the analysis involves providing the input data for the analysis and configuring the analysis parameters. The inputs for the analysis are as follows:

- a series of CT scans in DICOM format, which is a reference point in the registration process (pre-radiotherapy "planning CT" scans),
- a series of CT scans, in DICOM format, subject to transformation as part of the registration (follow-up CT scans, obtained at different timepoints after radiotherapy),
- information, in DICOM format, on the radiation doses delivered during treatment (RT Dose),
- information, in DICOM format, on contour data for treatment-relevant regions of interest (RT Structure).

In addition, as part of scheduling the analysis, it is necessary to indicate the dose range (in Gray units (Gy)) for which the analysis should be executed (areas limited by the isodose lines) and optionally the region of interest that should be included or excluded from it.

After scheduling the analysis, its related data is saved and execution is initialised as a DAG pipeline.

4.2. Pre-registration and registration

As presented in **Figure 5**: The entire analysis pipeline diagram presented as a directed acyclic graph (DAG) – screenshot, the pipeline starts with a pair of CT scans of the lungs, namely, a fixed image taken before radiotherapy and a moving image taken during the follow-up scan. The scans are stored in the standard form of a DICOM series, forming a three-dimensional

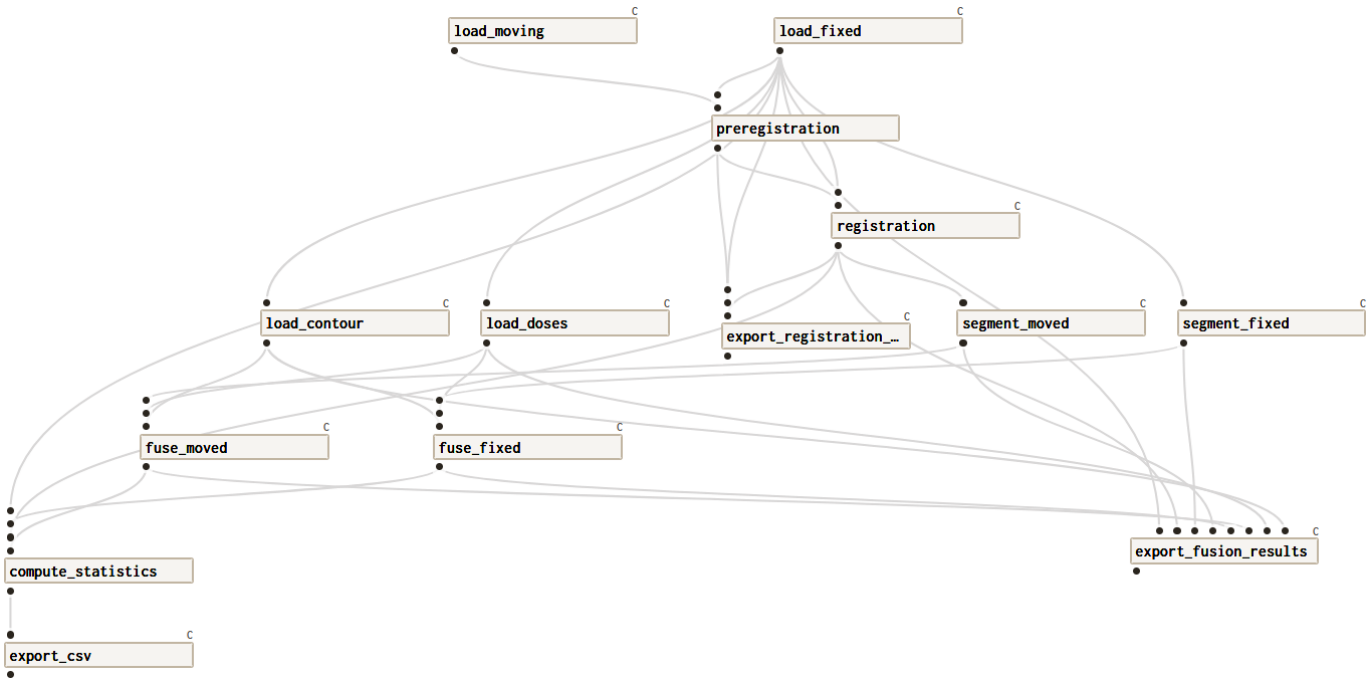

Figure 5. The entire analysis pipeline diagram presented as a directed acyclic graph (DAG) – screenshot.

cube. The first step of the processing pipeline is to load the scans. To avoid the loss of information, it was decided that a minimal level of pre-processing steps will be applied: no denoising, windowing, or isotropic voxel interpolation steps were used. Moreover, it was decided that the fixed image cannot undergo any transformation during the entire processing pipeline and all other processed entities are aligned with its specifications.

There are three main challenges in the registration of computed tomography (CT) of the lungs: large motion of small features, sliding motions between organs, and changing image contrast due to compression[41]. Most input pairs of scans differ in terms of global and local deformations, their size, and the physical spacing between voxels. Further stages of the processing pipeline require the unification of these properties; therefore, the next required step is the spatial alignment of the processed pair of scans. This family of problems is generally addressed by image registration algorithms.

In this particular pipeline, the image registration step was split into two sequential stages. First, non-deformable pre-registration, the main goal of which is to prepare the initial transformation. Second, the deformable registration, whose primary role is to provide a clinically correct alignment of the local non-rigid deformations between pair of scans.

Non-deformable image registration algorithms are considered fast and have relatively few parameters to optimise[42,43], therefore, breaking down the process described process into two disjoint steps acts as optimisation and aims to find the possibly best initial transformation for the deformable registration algorithm, which typically uses many orders of magnitude more degrees of freedom than non-deformable registration algorithms. In this specific implementation, the Image Registration Method from the SITK package was used. This method uses the centred transformation as an initial solution. Then iteratively using the gradient descent optimiser adjusts the initial trans formation matrix to optimise the given similarity function with the affine transformations constraint. Mutual information (MI) was used as a similarity function in this setup. Finally, the linear interpolator is used to resample the moving scan according to the resulting transformation matrix. This operation provides an approximation of a global alignment between the moving image and the fixed image and brings the moving image to the size and resolution of the fixed image.

The next step is the deformable registration algorithms, the main goal of which is local deformation alignment. Two types of method are currently present in the literature: deep learning and iterative. Deep learning registration methods have shorter processing times, but most often require separated training for each specific body part or modality. Iterative approaches, on the other hand, have longer processing times but have higher generalisation capabilities. It was decided that high generalisation capabilities are a highly desired feature in this presented system, so an iterative approach was chosen as the default. At the time of writing this article, the system supports only one algorithm (DEEDS), which was proposed in[41,44]. Its design is based on an intensity-driven minimum-spanning tree representation, discrete optimisation, a dense stochastic displacement sampling approach as a similarity function, and a diffeomorphic B-spline transformation model with diffusion regularisation[41]. The DEEDS algorithm reaches the state-of-the-art results of open source iterative approaches in[45,46].

As mentioned above, deformable registration algorithms typically have a large number of degrees of freedom. This directly affects their longer processing times. One of the factors that also heavily influences processing times is the size of the processed scans. Therefore, the registration step could be significantly optimised in terms of processing times by cropping the input scans only to areas that represent regions of interest (lungs). However, in this particular implementation, it was decided to keep the scans in their original field of view to give the algorithms full capabilities to use as much information as possible to ensure the anatomical correctness of the resulting transformations.

4.3. Extraction of desired regions

The resulting scans from the previous step reflect not only the lungs, but also the surrounding body parts. Only particular areas of the lungs that have been exposed to radiation are important in the presented analysis, so the lung areas will be segmented from the images of the previous stage, and then using the so-called fusion stage the lung areas of interest will be obtained.

In terms of segmentation, the system supports two solutions. The first is a convolutional neural network approach – the U-Net-based solution introduced in[47], which provides very precise results but at the same time requires substantial computing resources. The second solution is the heuristic segmentation method described in[23], which is based on the labelling of the connected components. Very brief tests indicated that the second approach is fast and robust enough to be used as the default segmentation solution in the presented analysis pipeline.

The masks created by segmentation are then passed to the so-called fusion operation. At this stage, three representations of the data – lung masks, doses, and optional contours – are fused into one. Based on these three representations, a target mask is generated, which will be used for further analysis steps. The mask is created by selecting the intersection part of the segmented lung areas and the lung areas that have been exposed to radiation doses. An optional operation at this step is to apply the contour in accordance with a previously configured logical operator.

4.4 Calculation and results preparation phase

The key element of the computational stage of the analysis is the calculation of the difference in radiodensity, for the assumed corresponding areas and for the assumed dose ranges, between two series of CT scans subject to analysis. The unit adopted in the calculations is the Hounsfield scale [HU], a quantitative scale that provides a density value for each type of tissue[48].

In the first step, the system reads the file with information in DICOM format, provided at the analysis configuration stage, on the radiation doses delivered during treatment (RT dose). Then, on the basis of that, the system creates a map of doses in relation to the first series of CT scans (reference point in the

analysis) and assumptions made when planning the analysis for the tested dose ranges. After the registration of the series of CT scans is complete, the created dose map is applied to the series of CT scans resulting from the registration. Then, based on comparison with the first series of CT scans, the difference in HU values is calculated between the series and for the areas covered by the dose map. In addition, during these operations, PNG files are created, showing the course of subsequent analysis stages in a user-friendly form. These files are later presented in the Lungs Radiomics Project Application subsystem as a supplement to the calculation results. The presentation of results is described in more detail in Section 5. Analysis results presentation.

In the last step, the results are exported to a CSV file containing the calculation results of the analysis in comparative terms, i.e.,

- for each CT scan of the first series (reference point in the registration):
  - minimum radiodensity [HU],
  - the maximum radiodensity [HU],
  - the average radiodensity [HU],
  - the radiosensity median [HU],
  - the standard deviation of radiodensity [HU],
  - significance of the CT scan for the entire calculation, expressed in the number of points covered by the adopted dose mask within the CT scan.
- for each CT scan of the series resulting from registration:
  - minimum radiodensity [HU],
  - the maximum radiodensity [HU],
  - the average radiodensity [HU],
  - the radiosensity median [HU],
  - the standard deviation of radiodensity [HU],
  - significance of the CT scan for the entire calculation, expressed in the number of points covered by the adopted dose mask within the CT scan.
- differences between the values mentioned above and the corresponding CT scans,
- aggregated above-mentioned values for the whole CT scan series, both initial and resulting from registration.

5. Analysis results presentation

The results of the analysis are presented both in visual and computational form. The calculations performed during the analysis are available to the analyst in the form of a CSV file that contains the data described in detail in Section 4.4. Calculation and results preparation phase.

Visual results of the analysis are available in two variants:

- the result of a series of CT scans registration,
- the result of applying a dose mask to a series of CT scans.

The analysis is carried out in three-dimensional space for the entire series of CT scans counted as a whole, while the presentation of the results, for clarity, is made in two-dimensional terms, based on the comparison of corresponding CT scans between series.

Figure 6: Analysis result – example of the registration result presentation for selected CT scans from both series shows an example of the presentation of the registration result for selected CT scans from both series. Starting from the left, the first two images show the slice after and before the radiotherapy, respectively. The third slice comes from the moved scan, which is the moving scan aligned to the fixed scan. The last two images are the heatmap representing the differences between the voxel intensities on the scans before and after alignment. Differences should represent post-radiotherapy changes; however, some artefacts must be considered.

Figure 7: Analysis result – example of the result presentation of applying a mask of doses for selected CT scans from

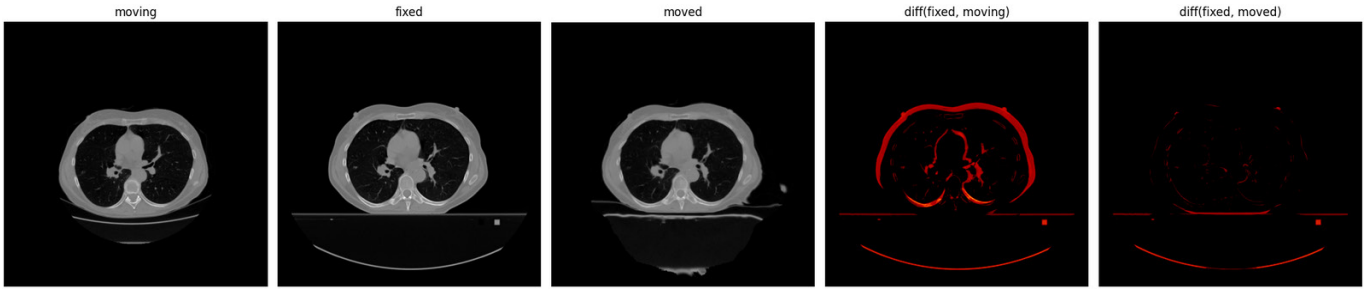

Figure 6. Analysis result – example of the registration result presentation for selected CT scans from both series.

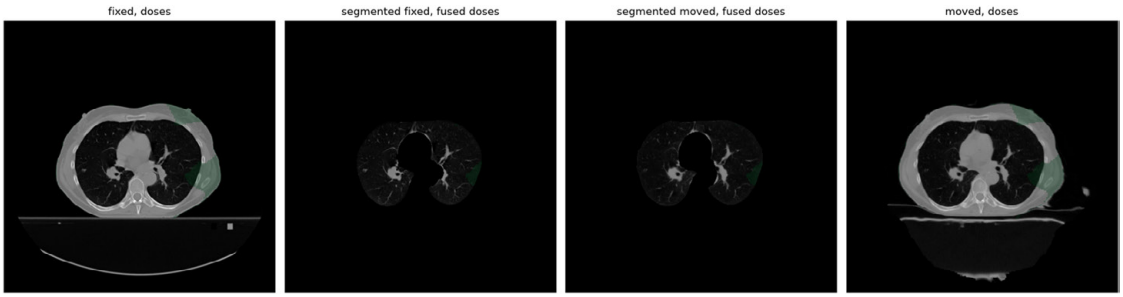

Figure 7. Analysis result – example of the result presentation of applying a mask of doses for selected CT scans from both series.

both series. shows an example of the presentation of the result of applying a dose mask for the same scans as in the previous figure. Images show green annotated radiation doses on pre and post-radiotherapy scans visualised on both segmented lung areas and raw scans. Looking from the left, the following can be observed:

- CT scan of the first series (reference point in the registration) with applied dose mask,
- segmented CT scan of the first series (reference point in the registration) with mask of doses applied,
- segmented CT scan from the second series (the one to which registration will be applied) with mask of doses applied, after registration,
- CT scan of the second series with mask of doses applied, after the registration.

6. System efficiency

As part of the system tests, a set of research data was used based on a series of CT scans for 50 patients. For each patient, at least two series of CT scans were performed, with an interval of at least three months, and then, using the system, an analysis of the series of scans was computed, comparing the first series of scans with subsequent series made for the same patient.

In total, 1598 analyses were performed. As part of the analyses, the following dose ranges were adopted:

- dose range from 0.1 Gy to 5 Gy – 214 analyses,
- dose range from 5.1 Gy to 10 Gy – 239 analyses,
- dose range from 10.1 Gy to 20 Gy – 230 analyses,
- dose range from 20.1 Gy to 30 Gy – 229 analyses,
- dose range from 30.1 Gy to 40 Gy – 228 analyses,
- dose range from 40.1 Gy to 50 Gy – 202 analyses,
- dose range from 50.1 Gy to 60 Gy – 168 analyses,
- dose range from 60.1 Gy to 70 Gy – 71 analyses,
- other dose ranges, less typical for the course of the experiment, 17 analyses.

The basic statistics on the execution time of the analyses can be depicted as follows:

- minimum execution time – 496 seconds,
- maximum execution time – 2200 seconds,
- average execution time – 1092.88 seconds,
- median execution times – 1064 seconds.

The distribution of the analysis execution times, in intervals of 250 ms, is shown in **Figure 8:** System efficiency – the distribution of analysis execution times.

The analyses were performed on a virtual machine equipped with the following parameters:

- 16 GB RAM
- 1000 GB HDD
- CPU Intel(R) Xeon(R) CPU E5-2680 v2 @ 2.80GHz, 4 cores.

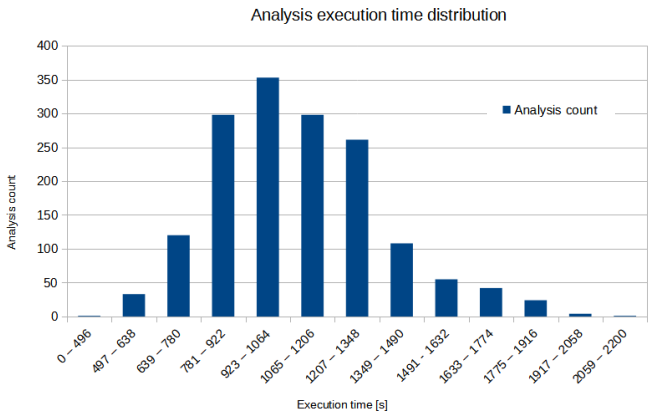

Figure 8. System efficiency – the distribution of analysis execution times

The execution times of the individual steps of the pipeline within the set of analyses, described above, are summarised in **Table 1**: Execution times of the pipeline steps. The average execution times of the subsequent steps of the pipeline are presented in **Figure 9**: System efficiency – the averaged times of execution of subsequent steps of the pipeline.

Table 1. Execution times of the pipeline steps.

Step	Min time [s]	Max time [s]	Avg time [s]
Fuse fixed images	below 0.01 s	1 s	below 0.01 s
Export statistics (CSV)	below 0.01 s	3 s	below 0.01 s
Load contours	below 0.01 s	3 s	0.02 s
Fuse moved images	below 0.01 s	9 s	0.07 s
Load fixed images	below 0.01 s	161 s	4.12 s
Load moving images	below 0.01 s	573 s	10.3 s
Compute statistics	5 s	71 s	11.61 s
Preregistration	10 s	134 s	48.39 s
Export registration results	25 s	538 s	52.51 s
Export fusion results	34 s	100 s	64.95 s
Load doses	below 0.01 s	886 s	86.69 s
Segment fixed images	48 s	134 s	94.93 s
Segment moved images	49 s	155 s	95.19 s
Registration	277 s	1038 s	624.11 s

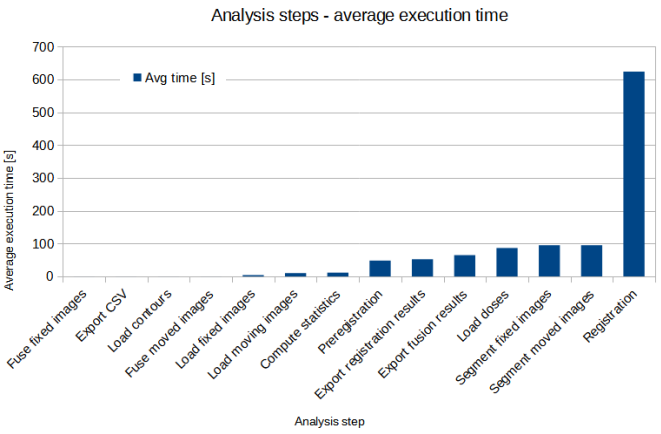

Figure 9. System efficiency – the averaged times of execution of subsequent steps of the pipeline.

7. Conclusions and future work

In this article, the current state of the system that allows one to automatically analyse changes in the patient's lung tissue density has been presented. The system now allows, thanks to the use of 3D registration algorithm, to analyse such changes more accurately than before, and thanks to the use of a more flexible and open to changes architecture, to introduce subsequent registration and calculation algorithms more easily.

In terms of performance, stability, and scalability of the system, the system is now more ready to perform analyses in parallel and, if necessary, to process large data sets and to introduce horizontal scaling mechanisms.

The two current main research and development areas of the system include:

- extension of the analytical capabilities of the system in the field of radiomics, in particular based on other than the first-order features used so far[13],
- expanding the number of image analysis algorithms used, in particular with algorithms based on deep learning mechanisms.

Changes in the areas mentioned above may allow the system to provide potentially more accurate results, which may open up new areas of application for the system within the area of medical imaging.

References

1. Bray F, Ferlay J, Soerjomataram I, Siegel RL, Torre LA, Jemal A. Global cancer statistics 2018: Globocan estimates of incidence and mortality worldwide for 36 cancers in 185 countries. CA: A Cancer Journal for Clinicians. 2018;68:394–424. doi:10.3322/CAAC.21492
2. Fitzmaurice C, Abate D, et al. Global, Regional, and National Cancer Incidence, Mortality, Years of Life Lost, Years Lived With Disability, and Disability-Adjusted Life-Years for 29 Cancer Groups, 1990 to 2017. JAMA Oncol. 2019;5(12):1749. doi:10.1001/jamaoncol.2019.2996
3. Zhang J, Li J, Xiong S, et al. Global burden of lung cancer: implications from current evidence. Ann Cancer Epidemiol. 2021;5:4-4. doi:10.21037/ace-20-31
4. Tyldesley S, Boyd C, Schulze K, Walker H, Mackillop WJ. Estimating the need for radiotherapy for lung cancer: an evidence-based, epidemiologic approach. International Journal of Radiation Oncology*Biology*Physics. 2001;49(4):973-985. doi:10.1016/s0360-3016(00)01401-2
5. Wei Z, Peng X, He L, Wang J, Liu Z, Xiao J. Treatment plan comparison of volumetric-modulated arc therapy to intensity-modulated radiotherapy in lung stereotactic body radiotherapy using either 6- or 10-MV photon energies. J Applied Clin Med Phys. 2022;23(8). doi:10.1002/acm2.13714
6. Ruysscher DD, Wauters E, Jendrossek V, et al. Diagnosis and treatment of radiation induced pneumonitis in patients with lung cancer: An ESTRO clinical practice guideline. Radiotherapy and Oncology. 2025;207:110837. doi:10.1016/j.radonc.2025.110837
7. Kolilekas L, Costabel U, Tzouvelekis A, Tzilas V, Bouros D. Idiopathic interstitial pneumonia or idiopathic interstitial pneumonitis: what's in a name? Eur Respir J. 2019;53(2):1800994. doi:10.1183/13993003.00994-2018
8. Arroyo-Hernández M, Maldonado F, Lozano-Ruiz F, Muñoz-Montaño W, Nuñez-Baez M, Arrieta O. Radiation-induced lung injury: current evidence. BMC Pulm Med. 2021;21(1). doi:10.1186/s12890-020-01376-4
9. Konkol M, Śniatała P, Milecki P. Radiation-induced lung injury — what do we know in the era of modern radiotherapy? Rep Pract Oncol Radiother. Published online March 31, 2022. doi:10.5603/rpor.a2022.0046
10. Käsmann L, Dietrich A, Staab-Weijnitz CA, et al. Radiation-induced lung toxicity – cellular and molecular mechanisms of pathogenesis, management, and literature review. Radiat Oncol. 2020;15(1). doi:10.1186/s13014-020-01654-9
11. Hu X, Bao Y, Xu Y, et al. Final report of a prospective randomized study on thoracic radiotherapy target volume for limited-stage small cell lung cancer with radiation dosimetric analyses. Cancer. 2019;126(4):840-849. doi:10.1002/cncr.32586
12. Hanania AN, Mainwaring W, Ghebre YT, Hanania NA, Ludwig M. Radiation-Induced Lung Injury. Chest. 2019;156(1):150-162. doi:10.1016/j.chest.2019.03.033
13. Mayerhoefer ME, Materka A, Langs G, et al. Introduction to Radiomics. J Nucl Med. 2020;61(4):488-495. doi:10.2967/jnumed.118.222893
14. Thomas R, Chen YH, Hatabu H, Mak RH, Nishino M. Radiographic patterns of symptomatic radiation pneumonitis in lung cancer patients: Imaging predictors for clinical severity and outcome. Lung Cancer. 2020;145:132-139. doi:10.1016/j.lungcan.2020.03.023
15. Choi YW, Munden RF, Erasmus JJ, et al. Effects of Radiation Therapy on the Lung: Radiologic Appearances and Differential Diagnosis. RadioGraphics. 2004;24(4):985-997. doi:10.1148/rg.244035160
16. Begosh-Mayne D, Kumar SS, Toffel S, Okunieff P, O'Dell W. The dose–response characteristics of four NTCP models: using a novel CT-based radiomic method to quantify radiation-induced lung density changes. Sci Rep. 2020;10(1). doi:10.1038/s41598-020-67499-0
17. Schröder C, Engenhart-Cabillic R, Kirschner S, Blank E, Buchali A. Changes of lung parenchyma density following high dose radiation therapy for thoracic carcinomas – an automated analysis of follow up CT scans. Radiat Oncol. 2019;14(1). doi:10.1186/s13014-019-1276-2
18. Bernchou U, Schytte T, Bertelsen A, Bentzen SM, Hansen O, Brink C. Time evolution of regional CT density changes in normal lung after IMRT for NSCLC. Radiotherapy and Oncology. 2013;109(1):89-94. doi:10.1016/j.radonc.2013.08.041
19. Defraene G, La Fontaine M, van Kranen S, et al. Radiation-Induced Lung Density Changes on CT Scan for NSCLC: No Impact of Dose-Escalation Level or Volume. International Journal of Radiation Oncology*Biology*Physics. 2018;102(3):642-650. doi:10.1016/j.ijrobp.2018.06.038
20. Palma DA, van Sörnsen de Koste J, Verbakel WFAR, Vincent A, Senan S. Lung Density Changes After Stereotactic Radiotherapy: A Quantitative Analysis in 50 Patients. International Journal of Radiation Oncology*Biology*Physics. 2011;81(4):974-978. doi:10.1016/j.ijrobp.2010.07.025
21. Al Feghali KA, Wu Q (Charles), Devpura S, et al. Correlation of normal lung density changes with dose after stereotactic body radiotherapy (SBRT) for early stage lung cancer. Clinical and Translational Radiation Oncology. 2020;22:1-8. doi:10.1016/j.ctro.2020.02.004
22. Ghobadi G, Wiegman EM, Langendijk JA, Widder J, Coppes RP, van Luijk P. A new CT-based method to quantify radiation-induced lung damage in patients. Radiotherapy and Oncology. 2015;117(1):4-8. doi:10.1016/j.radonc.2015.07.017
23. Konkol M, Śniatała K, Śniatała P, Wilk S, Baczyńska B, Milecki P. Computer Tools to Analyze Lung CT Changes after Radiotherapy. Applied Sciences. 2021;11(4):1582. doi:10.3390/app11041582

24. Konkol M, Bryl M, Fechner M, Matuszewski K, Śniatała P, Milecki P. Normal Lung Tissue CT Density Changes after Volumetric-Arc Radiotherapy (VMAT) for Lung Cancer. JPM. 2022;12(3):485. doi:10.3390/jpm12030485
25. Palmeri F, Zerunian M, Polici M, et al. Virtual biopsy through CT imaging: can radiomics differentiate between subtypes of non-small cell lung cancer? Radiol med. 2025;130(9):1363-1372. doi:10.1007/s11547-025-02022-x
26. Yang M, Shi L, Huang T, et al. Value of contrast-enhanced magnetic resonance imaging-T2WI-based radiomic features in distinguishing lung adenocarcinoma from lung squamous cell carcinoma with solid components >8 mm. J Thorac Dis. 2023;15(2):635-648. doi:10.21037/jtd-23-142
27. Gao S, Xu Z, Kang W, et al. Artificial intelligence-driven computer aided diagnosis system provides similar diagnosis value compared with doctors' evaluation in lung cancer screening. BMC Med Imaging. 2024;24(1). doi:10.1186/s12880-024-01288-3
28. Zhao W, Zou C, Li C, Li J, Wang Z, Chen L. Development of a diagnostic model for malignant solitary pulmonary nodules based on radiomics features. Ann Transl Med. 2022;10(4):201-201. doi:10.21037/atm-22-462
29. Ogbonna CP, Breen WG, Le Noach P, et al. Radiomics-based Prediction of Local Recurrence after Stereotactic Body Radiation Therapy for Early-Stage Non–Small Cell Lung Cancer. Annals ATS. 2025;22(8):1236-1243. doi:10.1513/annalsats.202410-1047oc
30. Salazar P, Cheung P, Ganeshan B, Oikonomou A. Predefined and data-driven CT radiomics predict recurrence-free and overall survival in patients with pulmonary metastases treated with stereotactic body radiotherapy. Faggioni L, ed. PLoS ONE. 2024;19(12):e0311910. doi:10.1371/journal.pone.0311910
31. Jiang Z, Li Q, Ruan J, et al. Machine Learning-Based Prediction of Pathological Responses and Prognosis After Neoadjuvant Chemotherapy for Non–Small-Cell Lung Cancer: A Retrospective Study. Clinical Lung Cancer. 2024;25(5):468-478.e3. doi:10.1016/j.cllc.2024.04.006
32. Wang F, Yang H, Chen W, et al. A combined model using pre-treatment CT radiomics and clinicopathological features of non-small cell lung cancer to predict major pathological responses after neoadjuvant chemoimmunotherapy. Current Problems in Cancer. 2024;50:101098. doi:10.1016/j.currproblcancer.2024.101098
33. Park JA, Pham D, Wang H, Khandhar S, Weyant MJ, Suzuki K. Radiomic score is prognostic in clinical stage I lung adenocarcinoma ≤2 cm undergoing surgery. J Thorac Dis. 2024;16(10):6475-6482. doi:10.21037/jtd-24-923
34. Niu Y, Jia HB, Li XM, et al. Deep learning radiomics and mediastinal adipose tissue-based nomogram for preoperative prediction of postoperative brain metastasis risk in non-small cell lung cancer. BMC Cancer. 2025;25(1). doi:10.1186/s12885-025-14466-5
35. Muccini H, Vaidhyanathan K. Software Architecture for ML-based Systems: What Exists and What Lies Ahead. 2021 IEEE/ACM 1st Workshop on AI Engineering - Software Engineering for AI (WAIN). Published online May 2021:121-128. doi:10.1109/wain52551.2021.00026
36. How to describe software architecture, https://wildasoftware.pl/post/how-describe-software-architecture, accessed: 2025-07-02
37. Github - dagster-io/dagster: An orchestration platform for the devel-opment, production, and observation of data assets., https://github.com/dagster-io/dagster, accessed: 2025-07-02
38. Mariadb foundation - mariadb.org, https://mariadb.org/, accessed: 2025-07-02
39. Welcome to python.org, https://www.python.org/, accessed: 2025-07-02
40. Lowekamp BC, Chen DT, Ibáñez L, Blezek D. The Design of SimpleITK. Front Neuroinform. 2013;7. doi:10.3389/fninf.2013.00045
41. Heinrich HP, Jenkinson M, Brady M, Schnabel JA. MRF-Based Deformable Registration and Ventilation Estimation of Lung CT. IEEE Trans Med Imaging. 2013;32(7):1239-1248. doi:10.1109/tmi.2013.2246577
42. Mani V, Selvaraj A. Survey of medical image registration, Journal of Biomedical Engineering and Technology. 2013;1:8-25
43. Maintz JBA, Viergever MA. A survey of medical image registration. Medical Image Analysis. 1998;2(1):1-36. doi:10.1016/s1361-8415(01)80026-8
44. Heinrich MP, Jenkinson M, Brady SM, Schnabel JA. Globally Optimal Deformable Registration on a Minimum Spanning Tree Using Dense Displacement Sampling. Lecture Notes in Computer Science. Published online 2012:115-122. doi:10.1007/978-3-642-33454-2_15
45. Liu F, Yan K, Harrison AP, et al. SAME: Deformable Image Registration Based on Self-supervised Anatomical Embeddings. Lecture Notes in Computer Science. Published online 2021:87-97. doi:10.1007/978-3-030-87202-1_9
46. Xu Z, Lee CP, Heinrich MP, et al. Evaluation of Six Registration Methods for the Human Abdomen on Clinically Acquired CT. IEEE Trans Biomed Eng. 2016;63(8):1563-1572. doi:10.1109/tbme.2016.2574816
47. Hofmanninger J, Prayer F, Pan J, Röhrich S, Prosch H, Langs G. Automatic lung segmentation in routine imaging is primarily a data diversity problem, not a methodology problem. Eur Radiol Exp. 2020;4(1). doi:10.1186/s41747-020-00173-2
48. Morar L, Băciuț G, Băciuț M, et al. Analysis of CBCT Bone Density Using the Hounsfield Scale. Prosthesis. 2022;4(3):414-423. doi:10.3390/prosthesis4030033